Supplementary Material for "Gate-defined topological Josephson junctions in Bernal bilayer graphene "

Ying-Ming Xie,[1,2,3] Étienne Lantagne-Hurtubise,[2,3], Andrea F. Young,[4] Stevan Nadj-Perge,[4,3], Jason Alicea,[2,3]

[1] *Department of Physics, Hong Kong University of Science and Technology, Clear Water Bay, Hong Kong, China*
[2] *Department of Physics, California Institute of Technology, Pasadena, California 91125, USA*
[3] *Institute for Quantum Information and Matter, California Institute of Technology, Pasadena CA 91125, USA*
[4] *Department of Physics, University of California at Santa Barbara, Santa Barbara CA 93106, USA*
[5] *T. J. Watson Laboratory of Applied Physics, California Institute of Technology, 1200 East California Boulevard, Pasadena, California 91125, USA*

I. MINIMAL MODEL FOR BLG AT FINITE DISPLACEMENT FIELDS

The four-band continuum model describing BLG under a perpendicular displacement field D can be written as

$$h_\tau(\boldsymbol{k}) = \begin{pmatrix} u/2 & v_0\Pi^\dagger & -v_4\Pi^\dagger & -v_3\Pi \\ v_0\Pi & \Delta'+u/2 & \gamma_1 & -v_4\Pi^\dagger \\ -v_4\Pi & \gamma_1 & \Delta'-u/2 & v_0\Pi^\dagger \\ -v_3\Pi^\dagger & -v_4\Pi & v_0\Pi & -u/2 \end{pmatrix}. \quad \text{(S1)}$$

On the left side, $\tau = \pm 1$ indicates the two valleys $\pm\boldsymbol{K} = (\pm\frac{4\pi}{3a}, 0)$, with a the lattice constant, and $\boldsymbol{k}$ denotes the momentum measured with respect to $\pm\boldsymbol{K}$. On the right side, $\Pi = (\tau k_x + ik_y)$ specifies the momentum; the basis is $\psi_\tau(\boldsymbol{k}) = (\psi_{\tau,A_1}(\boldsymbol{k}), \psi_{\tau,B_1}(\boldsymbol{k}), \psi_{\tau,A_2}(\boldsymbol{k}), \psi_{\tau,B_2}(\boldsymbol{k}))$ with A, B labeling the sublattice degree of freedom and $1, 2$ labeling the layer; and $v_j \equiv \frac{\sqrt{3}}{2}a\gamma_j$, γ_1, Δ', and u are band-structure parameters. Specifically, γ_j's encode various hopping processes, Δ' is an on-site potential difference resulting from the stacking, and $u = -d_\perp D/\epsilon_{\text{BLG}}$ is the energy difference between the two layers caused by the perpendicular displacement field D ($d_\perp = 0.33$ nm is the interlayer distance and $\epsilon_{\text{BLG}} \approx 4.3$ the relative permittivity of BLG.)

Parameters recovering first-principles band structures are given in Ref. 103: intralayer nearest-neighbor hopping is $\gamma_0 = 2.61$ meV; interlayer hoppings are $\gamma_1 = 361$ meV, $\gamma_3 = 283$ meV, $\gamma_4 = 138$ meV; and the onsite potential difference is $\Delta' = 15$ meV. In recent experiments, the D field yielding optimal superconductivity falls in the range of about $1 \sim 1.3$ V/nm, corresponding to an energy difference $u \approx$ 80-100 meV [37, 86]. We fix $u = 100$ meV in our simulations with $D \neq 0$. Figure S1 illustrates the BLG band structures at (a) zero and (b) nonzero displacement field.

In the main text, we proposed a minimal model for the valence band that captures the low-energy dispersion for hole-doped BLG near the Fermi energy in the presence of strong displacement fields:

$$h_0(\boldsymbol{k}) = -\mu + t_a\boldsymbol{k}^2 + t_c\boldsymbol{k}^4 + t_b(k_x^3 - 3k_xk_y^2)\tau_z. \quad \text{(S2)}$$

To estimate the effective parameters $t_{a,b,c}$, we compare the original bands obtained from $h_\tau(\boldsymbol{k})$ with those fitted by the proposed minimal model $h_0(\boldsymbol{k})$. We find that the dispersions roughly match with $t_a = 4$ eV$\cdot\, a^2$, $t_b = -60$ eV$\cdot\, a^3$, $t_c = -1500$ eV$\cdot\, a^4$; see the energies in Fig. S1(c) as well as the density of states and Fermi contours in Fig. S1(d,e).

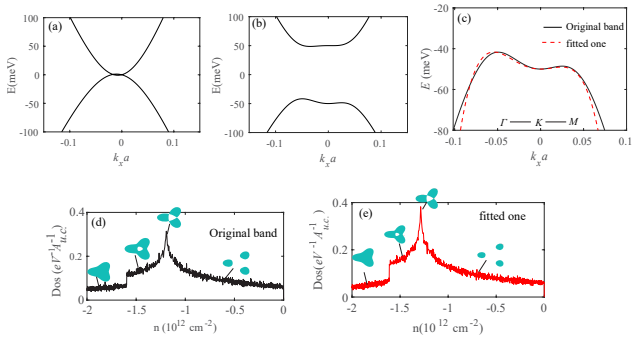

FIG. S1. (a,b) Low-energy bands of BLG in valley $+\boldsymbol{K}$ (a) without any displacement field and (b) with a displacement field giving $u = 100$ meV. (c) Valence-band energy E versus k_x in valley $+\boldsymbol{K}$ with $k_y = 0$ and a non-zero displacement field. Solid black line shows the dispersion obtained from the four-band model $h_+(\boldsymbol{k})$, while the dashed red line is a fit using the minimal model $h_0(\boldsymbol{k})$. (d,e) Density of states (Dos) versus hole density obtained from (d) the four-band model and (e) the minimal model, using temperature $T = 10$ mK for broadening. The insets show the topography of Fermi contours at various hole densities.

II. SPIN-ORBIT COUPLING IN THE MINIMAL MODEL

At the level of the four-band continuum model, Eq. (S1), the SOC terms appear as [37, 86, 108, 109]

$$h_{\text{SOC},\tau}(\boldsymbol{k}) = \mathcal{P}_1\left[\frac{\lambda_I}{2}\tau s_z + \frac{\lambda_R}{2}(\tau\zeta_x s_y - \zeta_y s_x)\right]. \quad \text{(S3)}$$

Here ζ and s are Pauli matrices acting on the sublattice (A, B) and spin degree of freedom, respectively, and $\mathcal{P}_1 = \text{diag}[1, 1, 0, 0]$ projects onto the top layer in the basis used to define Eq. (S1).

Ising and Rashba SOC terms behave very differently within the valence bands of interest. At least for $\boldsymbol{k}$ near zero, the BLG valence bands become strongly layer and

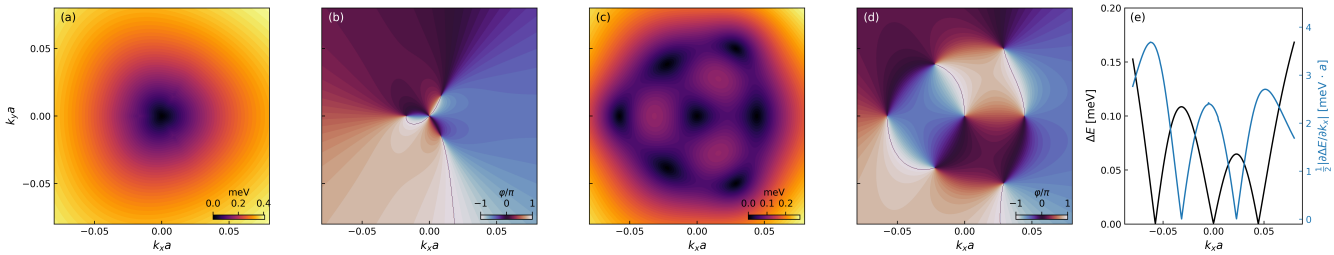

FIG. S2. Rashba SOC effects in the top-most valence band of BLG, in the absence of Ising SOC ($\lambda_I = 0$). We take $\lambda_R = 1$ meV in Eq. (S3), on the lower end of the experimentally reported range [86, 104–107]. Panels (a,b) correspond to BLG/WSe_2 at zero displacement field D, while panels (c-e) use $D \sim 1.3$ V/nm (corresponding to interlayer potential $u = 100$ meV). The energy difference ΔE between the Rasbha spin-split valence bands for momenta near the $\boldsymbol{K}$ point appears in (a,c); the associated spin winding for the top-most spin-split valence band, $\varphi \equiv \arg(\langle s_x\rangle + i\langle s_y\rangle)$, appears in (b,d). (e) Black line: one-dimensional cut through panel (c) for $k_y = 0$. Blue dots: derivative of the spin splitting ΔE along k_x (for $k_y = 0$), which gives a proxy for the parameter α_R defined in the main text [see Eq. (2)].

sublattice polarized by a strong D field. This polarization negligibly impacts λ_I but suppresses the effects of Rashba SOC due to the latter's off-diagonal structure in sublattice space. Hence, Rasbha coupling primarily manifests via virtual excitations to remote bands, which can be understood, e.g., using perturbation theory in the limit where trigonal warping is neglected and one considers a theory with a quadratic band touching at $D = 0$ (see Ref. 110). In reality, trigonal warping splits the band touching into four Dirac points at $D = 0$, around which the spins wind due to Rashba SOC; see Fig. S2(a) and (b). With a strong D field, the Rashba spin-splitting is suppressed and its texture becomes more complicated; see Fig. S2(c) and (d). The scale of the Rashba spin splitting strongly depends on whether the Fermi surface (in a given valley) comprises three small pockets or a single large pocket. Figure S2(e) shows a one-dimensional cut of the Rashba spin splitting along k_x with $k_y = 0$. As a proxy for the α_R parameter defined in Eq. (2), (one half of) the derivative of the Rashba spin-splitting as a function of k_x is shown in Fig. S2(e); note that the spin splitting will be *twice* the energy scale $\alpha_R k_x$. In the big Fermi pockets where $k_x a \sim 0.06$, we find that a typical scale for $\alpha_R \sim (1-3) \times \lambda_R \cdot a$. Conservatively estimating $\lambda_R \sim 1$ meV (on the lower end of the experimentally reported range [86, 104–107]), we then obtain $\alpha_R \sim 1 - 3$ meV $\cdot\, a$, corresponding to the range specified in the main text.

III. DETERMINING THE TOPOLOGICAL REGION WITH THE SCATTERING MATRIX METHOD

The solvable toy model for the planar Josephson junction described below Eq. (7) of the main text uses a piecewise-constant valence-band Hamiltonian

$$\tilde{H}_{\text{eff}}(k_x, y) = \frac{\partial_y^2 - k_x^2}{2m} - \mu(y) + \tilde{\alpha}_R(k_x\sigma_y + i\partial_y\sigma_x) + \tilde{h}\sigma_x \tag{S4}$$

with

$$\mu(y) = \mu_1\theta(L/2 - |y|) + \mu_2\theta(|y| - L/2). \tag{S5}$$

Above, θ is a step function and $\mu(y)$ captures the chemical potential profile across the device. For the pairing potential we take

$$\Delta(y) = \Delta e^{i\text{sgn}(y)\phi/2}\theta(|y| - L/2). \tag{S6}$$

The phase difference ϕ between the two superconductors can be controlled by applying current or magnetic flux through a loop connected to the junction [63, 64].

The onset of topological superconductivity in the barrier is most easily diagnosed by studying the ABS spectrum at $k_x = 0$. For convenience, we rearrange the basis as $(c_{k_x=0,\uparrow}, c_{k_x=0,\downarrow}, c^\dagger_{-k_x=0,\downarrow}, -c^\dagger_{-k_x=0,\uparrow})^T$ so that the $k_x = 0$ BdG Hamiltonian becomes

$$H_{BdG} = \left[\frac{\partial_y^2}{2m} - \mu(y) + \tilde{h}\sigma_x\right]\rho_z + i\tilde{\alpha}_R\partial_y\sigma_x\rho_z + \text{Re}\Delta(y)\rho_x + \text{Im}\Delta(y)\rho_y, \tag{S7}$$

where ρ are Pauli matrices that act in particle-hole space. The analysis is streamlined by the fact that, at $k_x = 0$, the BdG Hamiltonian in the preceding basis commutes with $\eta \equiv \sigma_x$. In sector $\eta = \pm 1$, the Hamiltonian reduces to a 2×2 matrix

$$H_\eta = \begin{pmatrix} \xi(y) + i\eta\tilde{\alpha}_R\partial_y + \eta\tilde{h} & \Delta(y) \\ \Delta(y)^* & -\xi(y) - i\eta\tilde{\alpha}_R\partial_y + \eta\tilde{h} \end{pmatrix} \tag{S8}$$

with $\xi(y) = \partial_y^2/(2m) - \mu(y)$. Next, we find the ABS energies using scattering matrix formalism.

In the barrier region ($\Delta = 0$, $\mu = \mu_1$), the energies are $\epsilon = \pm[-k_y^2/(2m) - \mu_1] \pm \eta\tilde{\alpha}_R k_y + \eta\tilde{h}$ with associated

TABLE S1. Classification of possible translation-invariant IVC order parameters, and other types of order parameters for comparison, based on time-reversal $\mathcal{T}$, C_3 rotation, mirror operation $M_x = i\tau_x s_x$, and $U_v(1)$ rotation symmetries.

Δ_n	$\mathcal{T} = i\tau_x s_y K$	$C_3 = e^{-i\frac{\pi}{3}s_z}$	$M_x = i\tau_x s_x$	$U_v(1) = e^{i\varphi\tau_z}$	comment
$\tau_x(s_x, s_y)$	-1	(x, y)	$(+1, -1)$	no	nematic IVC
$\tau_y(s_x, s_y)$	-1	(x, y)	$(-1, +1)$	no	nematic IVC
$\tau_x s_0$	$+1$	$+1$	$+1$	no	IVC
$\tau_x s_z$	-1	$+1$	-1	no	spin-valley intertwined IVC
$\tau_y s_0$	$+1$	$+1$	-1	no	IVC
$\tau_y s_z$	-1	$+1$	$+1$	no	spin-valley intertwined IVC
$\tau_z(s_x, s_y)$	$+1$	(x, y)	$(-1, +1)$	yes	nematic valley polarized
$\tau_z s_0$	-1	$+1$	-1	yes	valley polarized
$\tau_z s_z$	$+1$	$+1$	$+1$	yes	spin-valley polarized
$\tau_0(s_x, s_y)$	-1	(x, y)	$(+1, -1)$	yes	nematic spin-polarized
$\tau_0 s_z$	-1	$+1$	-1	yes	spin polarized
$(k_x, k_y)\tau_x(s_x, s_y)$	$+1$	$(x, y) \times (x, y)$	$(-1, +1) \times (+1, -1)$	no	spin-orbit-valley intertwined IVC
$(k_x, k_y)\tau_y(s_x, s_y)$	$+1$	$(x, y) \times (x, y)$	$(-1, +1) \times (-1, +1)$	no	spin-orbit-valley intertwined IVC
$(k_x, k_y)\tau_y s_z$	$+1$	(x, y)	$(-1, +1)$	no	spin-orbit-valley intertwined IVC
$(k_x, k_y)\tau_x s_z$	$+1$	(x, y)	$(+1, -1)$	no	spin-orbit-valley intertwined IVC

wavefunctions

$$\psi^{\nu}_{e,\eta} = \begin{pmatrix} 1 \\ 0 \end{pmatrix} e^{ik^{\nu}_{F,e}y}, \tag{S9}$$

$$\psi^{\nu}_{h,\eta} = \begin{pmatrix} 0 \\ 1 \end{pmatrix} e^{ik^{\nu}_{F,h}y}, \tag{S10}$$

where

$$k^{\nu}_{F,e} = \eta m\tilde{\alpha}_R + \nu\sqrt{m^2\tilde{\alpha}_R^2 + 2m(\eta\tilde{h} - \epsilon - \mu_1)} \tag{S11}$$

$$k^{\nu}_{F,h} = \eta m\tilde{\alpha}_R - \nu\sqrt{m^2\tilde{\alpha}_R^2 - 2m(\eta\tilde{h} - \epsilon + \mu_1)} \tag{S12}$$

and $\nu = \pm$ labels the right versus left movers.

In the superconducting regions ($\Delta \neq 0$, $\mu = \mu_2$), the wavefunctions are instead

$$\psi'^{\nu}_{e,\eta} = \frac{1}{\sqrt{2}} \begin{pmatrix} e^{i\mathrm{sgn}(y)\phi/2} \\ e^{-i\gamma} \end{pmatrix} e^{ik^{\nu}_{S,e}y} \tag{S13}$$

$$\psi'^{\nu}_{h,\eta} = \frac{1}{\sqrt{2}} \begin{pmatrix} e^{i\mathrm{sgn}(y)\phi/2} \\ e^{i\gamma} \end{pmatrix} e^{ik^{\nu}_{S,h}y}, \tag{S14}$$

where $\gamma = \arccos\left(\frac{\epsilon - \eta\tilde{h}}{\Delta}\right)$,

$$k^{\nu}_{S,e} = k^{\nu}_{F,e} + \frac{i\nu\sqrt{\Delta^2 - (\eta\tilde{h} - \epsilon)^2}}{\sqrt{m^2\tilde{\alpha}_R^2 + 2m(\eta\tilde{h} - \epsilon - \mu_2)}} \tag{S15}$$

$$k^{\nu}_{S,h} = k^{\nu}_{F,h} + \frac{-i\nu\sqrt{\Delta^2 - (\eta\tilde{h} - \epsilon)^2}}{\sqrt{m^2\tilde{\alpha}_R^2 - 2m(\eta\tilde{h} - \epsilon + \mu_2)}}. \tag{S16}$$

With the above modes, it is straightforward to obtain the scattering matrix according to Refs. 111 and 112. We first focus on the case with a uniform chemical potential in the junction and superconducting regions, i.e., $\mu_1 = \mu_2 = \mu$. In the Andreev limit $|\mu| \gg (\Delta, B)$, the reflection matrices at the left interface r_{L} and right interface r_{R}, and transmission matrices (left to right as t_{RL} and right to left as t_{LR}) are

$$r_{\mathrm{L}} = \begin{pmatrix} 0 & e^{-i\gamma - i\frac{\phi}{2}} \\ e^{-i\gamma + i\frac{\phi}{2}} & 0 \end{pmatrix}, r_{\mathrm{R}} = \begin{pmatrix} 0 & e^{-i\gamma + i\frac{\phi}{2}} \\ e^{-i\gamma - i\frac{\phi}{2}} & 0 \end{pmatrix}, \tag{S17}$$

$$t_{\mathrm{LR}} = \begin{pmatrix} e^{ik^{+}_{F,e}L} & 0 \\ 0 & e^{ik^{+}_{F,h}L} \end{pmatrix}, t_{\mathrm{RL}} = \begin{pmatrix} e^{-ik^{-}_{F,e}L} & 0 \\ 0 & e^{-ik^{-}_{F,h}L} \end{pmatrix}. \tag{S18}$$

The ABSs energies ϵ_n can be solved from $\mathrm{Det}[1 - r_{\mathrm{L}}t_{\mathrm{LR}}r_{\mathrm{R}}t_{\mathrm{RL}}] = 0$, which gives

$$\cos[2\beta_m L - 2\gamma] = \cos(\phi). \tag{S19}$$

Here, $\beta_m = \frac{k^{+}_{F,e} - k^{-}_{F,h}}{2} \approx \frac{\eta\tilde{h} - \epsilon}{v_F}$. The main text Eq. (8) then follows by considering the short-junction limit where the Thouless energy satisfies $E_T = \frac{\pi v_F}{2L} \gg \Delta, h$.

Now we examine the case with a chemical potential difference $\mu_1 \neq \mu_2$. The transmission matrices t_{LR} and t_{RL} keep the same form as above, though the reflection matrices now encode additional normal reflections. The matrix r_{L} can be written as

$$r_{\mathrm{L}} = \begin{pmatrix} ire^{i\theta_0} & \sqrt{1 - r^2}e^{i\theta_0}e^{-i\frac{\phi}{2}} \\ \sqrt{1 - r^2}e^{i\theta_0}e^{i\frac{\phi}{2}} & ire^{i\theta_0} \end{pmatrix}, \tag{S20}$$

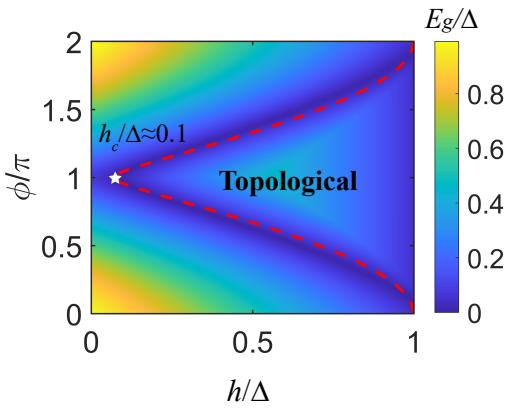

FIG. S3. The $k_x = 0$ gap E_g as a function of the Zeeman energy h and phase difference ϕ calculated from the tight-binding model reviewed in Sec. V. Parameters used are the same as in the main text Fig. 3(c), except that $\mu_1 = 3$ meV. The red dashed lines are obtained from Eq. (S24) with a normal reflection coefficient $r = 0.1$, while the white star indicates the critical field at $\phi = \pi$ extracted from the tight-binding model.

where

$$re^{i\theta_0} = \frac{2\sin\gamma(k_1^2 - k_2^2)}{(k_1+k_2)^2 e^{i\gamma} + (k_1^2 - k_2^2)e^{-i\gamma}}, \quad \text{(S21)}$$

$$\sqrt{1-r^2}e^{i\theta_0} = \frac{4k_1k_2}{(k_1+k_2)^2 e^{i\gamma} + (k_1^2 - k_2^2)e^{-i\gamma}}, \quad \text{(S22)}$$

and $k_{1,2} \approx \sqrt{m^2\tilde{\alpha}_R^2 + 2m|\mu_{1,2}|}$. If $\mu_1 = \mu_2$, one finds that $r = 0$ and $\theta_0 = -\gamma$, thus recovering the preceding results. The reflection matrix r_R can be obtained by replacing $\phi \to -\phi$ in r_L. One can readily verify unitarity of the reflection matrices r_L and r_R.

By solving $\mathrm{Det}[1 - r_L t_{RL} r_R t_{LR}] = 0$, we find that ABSs energies are determined by

$$\cos(2\theta + 2\beta_m L) + r^2\cos(2\beta_p L) = (1-r^2)\cos(\phi). \quad \text{(S23)}$$

Here, the average Fermi wavelength between the left-moving and right-moving states reads $\beta_p = \frac{k^+_{F,e} - k^-_{F,e}}{2} \approx k_1$. In the short junction limit with weak normal reflections, we can approximate Eq. (S23) as

$$\cos(2\gamma) = (1-r^2)\cos(\phi). \quad \text{(S24)}$$

Near $\phi = \pi$, we can roughly obtain the topological phase transition line as $\tilde{h}/\Delta = |\cos(\phi/2)| + r/\sqrt{2}\sin(\phi/2)$.

Let us compare the topological transition line given by Eq. (S24) to our tight-binding model calculation (see Sec. V later), as we have done for the main text Fig. 3(c). In Fig. 3(c), the chemical potential difference between the superconducting and barrier regions does not produce obvious effects. Here, we instead choose $\mu_1 = 3$ meV, $\mu_2 = -1$ meV to amplify the role of chemical potential mismatch. In this case, the gap E_g (extracted from the tight-binding model) as a function of Zeeman energy h and phase difference ϕ is shown in Fig. S3. Note that the effective Zeeman energy felt by the partially occupied bands is weakly renormalized (i.e., $\tilde{h} \approx h$) when $\lambda_0 \gg \beta_I$, as arises here. The red line is calculated from Eq. (S24) with a normal reflection magnitude $r = 0.1$, which shows good agreement with the phase transition line indicated by E_g. The dominant change to the phase diagram occurs near $\phi = \pi$, where a finite Zeeman energy of $r\Delta/\sqrt{2}$ is now needed to drive the junction into the topological phase, contrary to the $r = 0$ case where arbitrarily weak fields suffice.

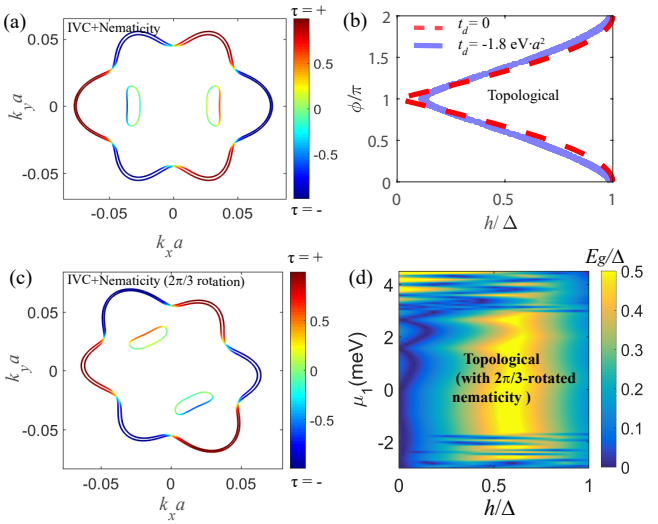

FIG. S4. (a,c) Fermi contours in the presence of finite nematicity modeled with $t_d = -3$ eV $\cdot a^2$. Panel (c) differs from (a) by a $2\pi/3$ rotation on the nematicity direction. Other parameters are the same as for the main text Fig. 2(c). (b) Topological phase transition lines in the case with nematicity ($t_d = -1.8$ eV$\cdot a^2$) and without nematicity ($t_d = 0$). Other parameters are the same as for the main text Fig. 3(f). Near $\phi = \pi$, the critical magnetic field to enter into the topological regions is modified slightly due to normal reflections enhanced by $t_d \neq 0$ in this case. (d) Gap E_g versus h and μ_1 obtained assuming the Fermi surface structure from (c). Other parameters are the same as for the main text Fig. 3(d).

IV. INCORPORATING NEMATICITY

Experiments [37, 38] suggest that the number of small Fermi pockets present in the superconducting regime may be smaller than six due to nematicity. To phenomenologically incorporate such effects, we explicitly break C_3 symmetry by replacing $\xi_0(\boldsymbol{k}) \to \xi_0(\boldsymbol{k}) + t_d k_y^2$ in $h_0(\boldsymbol{k})$ from the main text. Figure S4(a) illustrates the resulting Fermi contours—which for chemical potential and t_d value used exhibits only two small pockets. In the range $t_d \sim -6$ to -1.5 eV$\cdot a^2$, the Fermi pockets look similar: large pockets plus two small pockets near $k_y = 0$. A smaller t_d would introduce other small pockets, while a

larger t_d would dramatically distort the large pockets. We also verified that the chemical potential window at which the Fermi surface hosts only large Fermi pockets is only weakly affected by the introduction of t_d. The influence of nematicity (modeled in this fashion) on the topological region in the h-ϕ and h-μ_1 planes appear in Fig. S4(b) and the main text Fig. 3(e), respectively. It can be seen that the nematicity does not appreciably affect the topological region in the h-ϕ plane. However, the robust topological region significantly broadens in the h-μ_1 plane by removing the small pockets near $k_x = 0$ through the presence of nematicity.

In the preceding analysis we explicitly specified which two of the six small pockets remained in the presence of nematicity. In principle, one can rotate the nematicity direction so that a different pair of two small pockets appears near Fermi energy. We find that the robust topological regime is mainly hampered by states near zero momentum along the junction (in our setup near $k_x = 0$). In other words, provided the presence of nematicity can remove those states efficiently—which we find holds when the nematicity is strong enough to keep only two small pockets—the robust topological regime would be enlarged. Figure S4(c) illustrates a different set of two small pockets after a $2\pi/3$ rotation of the nematicity direction $[t_d k_y^2 \mapsto t_d(\frac{\sqrt{3}}{2}k_x + \frac{1}{2}k_y)^2]$ with respect to Fig. S4(a); as seen in Fig. S4(d), in this case a robust topological regime appears for $\mu_1 \sim (-2, 3)$ meV resembling that in the main text Fig. 3(e).

V. EFFECTIVE TIGHT-BINDING HAMILTONIAN FOR BLG/WSE2 JOSEPHSON JUNCTION

The tight-binding Hamiltonian used in the main text is deduced from the mean-field Hamiltonian Eq. (7) via a partial Fourier transform along y-direction. As an illustration, we present the resulting tight-binding Hamiltonian where the y-direction (perpendicular to the junction) is open while k_x is still a good quantum number. This tight-binding Hamiltonian can be written as

$$
\begin{aligned}
H_{tb} = \sum_j \Big\{ & \Psi^\dagger_{k_x,j} \Big[\big((t_a + 4t_c)k_x^2 + t_c k_x^4 - \mu_j + E_0\big) + \big(t_b k_x^3 - 6t_b k_x\big)\tau_z + \frac{\beta_I}{2}\tau_z s_z + \alpha_R k_x s_y + \lambda_0 \tau_x + \lambda_1 k_x s_y + h s_x \Big] \Psi_{k_x,j} \\
& + \Psi^\dagger_{k_x,j} \Big[-\big(t_a + t_d + 2t_c k_x^2 + 4t_c\big) + 3t_b k_x \tau_z - \frac{\alpha_R}{2i} s_x - \frac{\lambda_1}{2i}\tau_x s_x \Big] \Psi_{k_x,j+1} + t_c \Psi^\dagger_{k_x,j} \Psi_{k_x,j+2} \Big\} \\
& + \sum_{j<-L/2} \Delta e^{i\phi/2} \Psi^\dagger_{k_x,j} (i\tau_x s_y) \Psi^\dagger_{-k_x,j} + \sum_{j>L/2} \Delta e^{-i\phi/2} \Psi^\dagger_{k_x,j} (i\tau_x s_y) \Psi^\dagger_{-k_x,j} + \text{H.c.}
\end{aligned}
\tag{S25}
$$

Here, j labels lattice sites along the y direction ($j = 0$ corresponds to the middle of the junction); the four-component annihilation operator is $\Psi_{k_x,j} = (c_{+\uparrow,j}(k_x), c_{+\downarrow,j}(k_x), c_{-\uparrow,j}(k_x), c_{-\downarrow,j}(k_x))^T$; the chemical potential is $\mu_j = \mu_2\theta(|j|a - L/2) + \mu_1\theta(L/2 - |j|a)$, and $E_0 = 2(t_a + t_d) + 6t_c$ is a constant energy shift. We have defined the pairing matrix as $i\tau_x s_y$, which is an intervalley spin-singlet pairing. After projecting into the low-energy subspace spanned by Pauli matrices σ_i, this pairing takes the form $i\sigma_y$ as defined in the main text.

A similar calculation using a tight-binding model to simulate the continuum model can be found in Refs. 112 and 113. Figures 3 and 4 of the main text and Figs. (S3 to S7) of the supplemental material are obtained from the above tight-binding model Hamiltonian H_{tb}. IVC order, when present, is always taken to be position-independent for simplicity, e.g., we assume that it is also present in the barrier of the gate-defined Josephson junction.

VI. THE MINIMAL TOPOLOGICAL GAP IN VARIOUS PARAMETER REGIONS

Figure S5(a) illustrates the k_x-dependent ABS spectrum for a topological phase with $\phi = \pi$ and $h = 0.8\Delta$. Notice that the $k_x = 0$ gap E_g exceeds the minimal gap $E_{g,m}$. The $E_{g,m}$ gap—which limits the decay length of MZMs in the barrier—typically arises at finite k_x [Fig. S5(a)] and depends on various model parameters as shown in Fig. S5(b-d). In our simulations the optimal $E_{g,m}$ approaches $\sim 0.2\Delta$ and tends to occur (i) over a broad range of lengths ($L \sim 50 - 200$ nm) in the short-junction regime; (ii) for $\mu_1 \sim 0 - 3$ meV, where the barrier region is devoid of small Fermi pockets; and (iii) when Rashba coupling energy $\alpha_R k_F$ is sufficiently large relative to Ising SOC. Requirement (iii) follows from the fact that Ising SOC renormalizes downward the effective Rashba SOC for the relevant large Fermi surfaces; recall Eq. (6) in the main text.

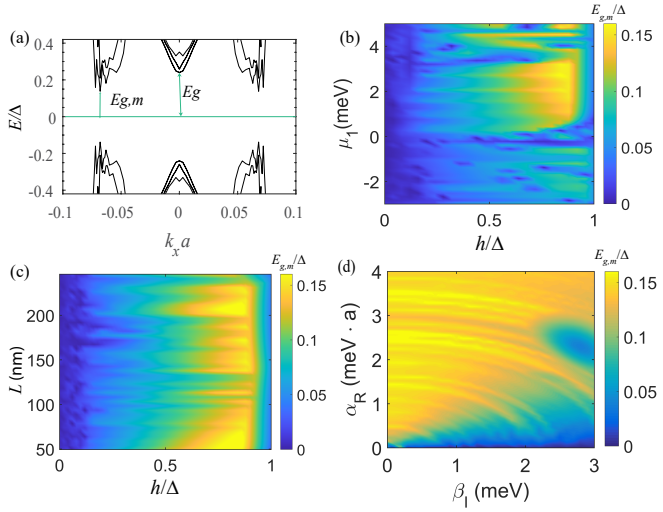

FIG. S5. (a) ABS spectrum versus k_x obtained from the tight-binding model [Eq. (S25)] with Zeeman field $h = 0.8\Delta$. The gap E_g at $k_x = 0$ and the minimal gap $E_{g,m}$ are highlighted. (b-d) Dependence of $E_{g,m}$ on various junction parameters. Data correspond to $L = 78$ nm, $\mu_1 = 2$ meV, $\mu_2 = -1$ meV, $\beta_I = 1.4$ meV, $\alpha_R = 2\text{meV} \cdot a$, $\lambda_0 = 3$ meV, $\lambda_1 = 0$, $h = 0.8\Delta$, and $\phi = \pi$.

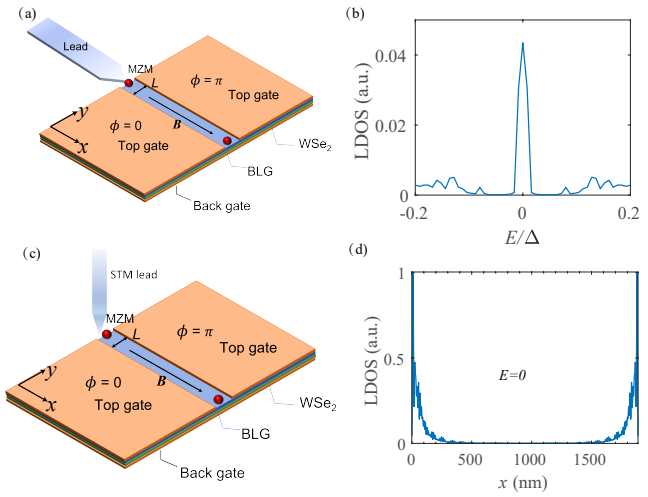

FIG. S6. (a,c) Illustration of detection schemes for Majorana zero-energy modes (MZMs) in the BLG/WSe_2 planar Josephson junction. (b,d) Local density of states (LDOS) that roughly mimics the conductance measured in the setups from (a,c). Panel (b) shows the energy dependence of the LDOS near the end of the barrier in the topological phase of the Josephson junction. The zero-bias peak originates from the MZM localized at the boundary. Panel (d) shows the position dependence of the zero-energy LDOS within the barrier—which maps the spatial structure of the Majorana modes. Data in (b,d) were obtained assuming the following: $L = 50$ nm, $\mu_1 = 2$ meV, $\mu_2 = -1$ meV, $\beta_I = 1.4$ meV, $\alpha_R = 2\text{meV} \cdot a$, $\lambda_0 = 3$ meV, $\lambda_1 = 0$, $h = 0.8\Delta$,$\phi = \pi$, and broading parameter $\eta = i\Delta/1000$.

VII. TUNNELING SPECTROSCOPY AND MAJORANA ZERO-MODES

The topological phase of the BLG/WSe_2 planar Josephson junction hosts a single MZM localized to each end of the barrier. Tunneling constitutes a commonly deployed—though subtle to interpret unambiguously—experimental tool for diagnosing the presence of Majorana modes. Figure S6(a,c) sketches two possible transport experiments to which our setup is amenable: (a) tunneling spectroscopy from a lead directly into the end of the barrier and (c) scanning tunneling microscopy (STM) that probes the full spatial extent of the barrier. The lead in (a) could in principle arise from the BLG/WSe_2 medium itself upon introducing appropriate tunnel barriers via gates; while STM offers a broader spatial field of view, the accessible temperatures are comparatively high, possibly on the scale of or larger than the topological gap for the junction. In this section we examine the LDOS in the barrier—which is expected to roughly track the conductances measured in such tunneling experiments. The LDOS at sites $\boldsymbol{r}_j$ is obtained from the Green's functions

$$\rho_{\text{LDOS}}(\boldsymbol{r}_j) = -\frac{1}{\pi}\text{Im}\{\text{tr}\,[G(\boldsymbol{r}_j)]\}. \tag{S26}$$

Here, $G(\boldsymbol{r}_j)$ denotes the Green's function at site $\boldsymbol{r}_j$, and the trace is taken over the valley and spin space. The LDOS is evaluated on a discrete grid of positions $\boldsymbol{r}_j$ used to define the effective tight-binding model Eq. S25—a discretized version of the low-energy continuum Hamiltonian in the main text. In the next section, we will show how to recover the full atomically resolved LDOS by introducing Wannier functions to describe atomic orbitals.

We obtain the LDOS from our tight-binding model [Eq. (S25)] by Fourier also transforming along the x direction, taking open boundary conditions to introduce endpoints for the barrier, and using the lattice Green's function method [112, 113] to obtain the Green's function $G_{nn}(E) = (E - H_{nn} - \Sigma + i\eta)^{-1}$ of the column representing the middle of the junction region, i.e., $y = 0$, where H_{nn} is the Hamiltonian of $n-$th column, Σ is the self-energy due to the coupling between nearest columns, and η is a broading parameter. See the caption of Fig. S6 for parameters. Figure S6(b) presents the energy dependence of the LDOS evaluated near the end of the barrier. The pronounced zero-bias peak reflects the associated localized MZM, and is the counterpart of the (quantized) zero-bias peak that would arise at zero temperature in the transport setup from panel (a). Figure S6(d) shows the spatial profile of the LDOS at zero energy, which is relevant for the STM setup from panel (b). Well-localized MZM wavefunctions—one from each end—are clearly visible; with the (not unreasonable) parameters used here, the decay length is on the 100 nm scale.

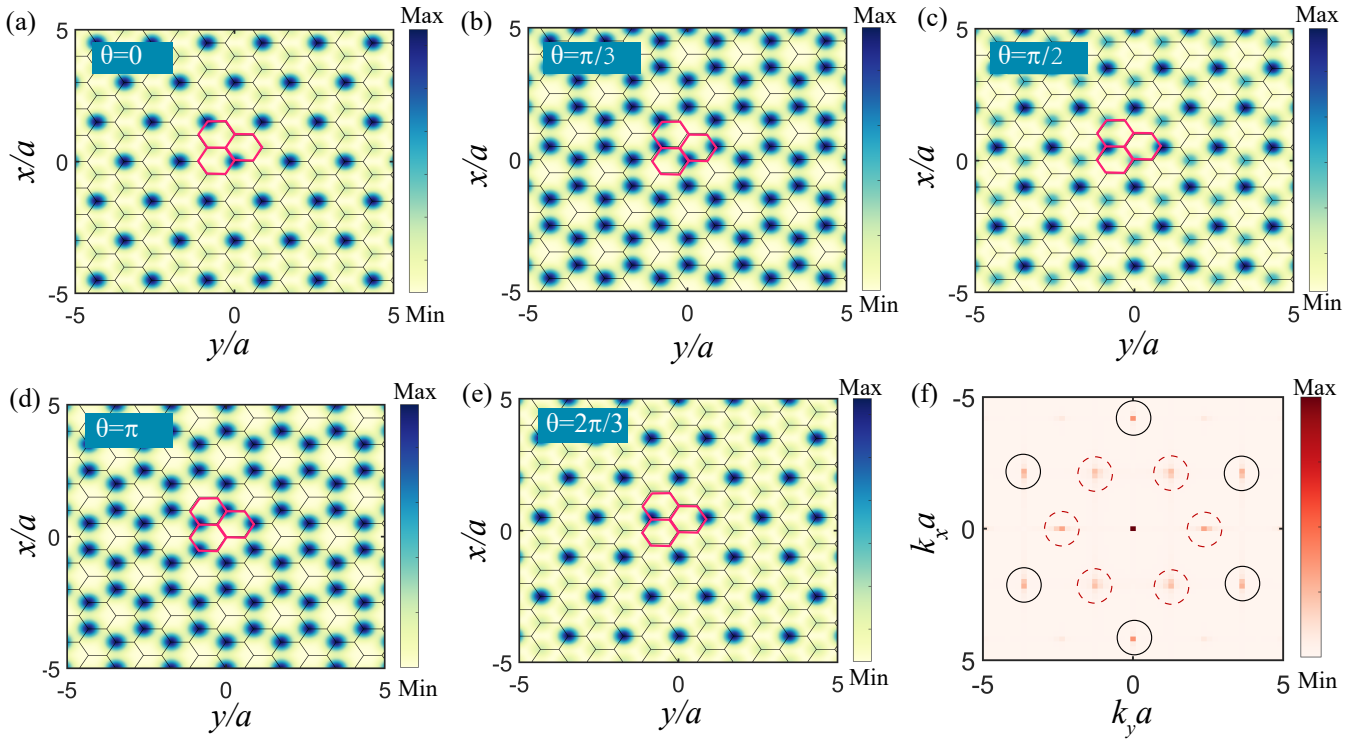

FIG. S7. (a-e) Kekulé patterns obtained from extended bulk states with energy $E = 1.2\Delta$ at various Kekulé angles θ. Three graphene hexagonal plaquettes are highlighted in pink color, which forms a Kekulé supercell. Note that mirror symmetry M_x is preserved only for $\theta = 0$ and π which correspond to a τ_x IVC order parameter (see SM Table S1). (f) Fourier transform of data in (a) for $\theta = 0$ (other angles exhibit similar features). Kekulé peaks are highlighted with red dashed circles.

VIII. COMPUTING ATOMICALLY RESOLVED MAJORANA ZERO MODE WAVEFUNCTIONS

The formalism of the previous section allows us to evaluate a 'coarse-grained' version of the LDOS, which captures the broad features of the low-energy wavefunctions but disregards atomically resolved information. We can capture the finer, atomic-scale structure of the LDOS by invoking Wannier functions that describe the relevant atomic orbitals. As shown in the main text, the necessity of IVC order to obtain topological superconductivity in our setup endows MZM wavefunctions with atomic-scale fingerprints, potentially detectable via STM. In this section, we explain the method used to compute those atomically resolved MZM wavefunctions.

For the purposes of this section, we parametrize the (spin-unpolarized) IVC order parameter as

$$\Delta_{\text{IVC}} = \cos(\theta)\tau_x + \sin(\theta)\tau_y, \tag{S27}$$

where θ denotes the Kekulé angle. Except for Fig. 4 of the main text, a τ_x order parameter (which respects the mirror symmetry M_x) was assumed, corresponding to $\theta = 0$. Different values of θ are contrasted in Fig. 4 to aid with experimental identification of IVC orders.

The LDOS, now including atomic-scale structure, is given by

$$\rho(E, \boldsymbol{r}) = -\frac{1}{\pi}\text{Im}\sum_n \frac{|\psi_n(\boldsymbol{r})|^2}{E - E_n + i\eta} \tag{S28}$$

where $\eta > 0$ is a small broadening parameter and $\psi_n(\boldsymbol{r})$ is the wavefunction for an eigenstate with energy E_n in the n-th band,

$$\psi_n(\boldsymbol{r}) = \sum_{\boldsymbol{r}_\alpha,\tau,s} c_{n,\tau,s}(\boldsymbol{r}_\alpha) e^{i\boldsymbol{K}_\tau\cdot\boldsymbol{r}_\alpha}\phi_\alpha(\boldsymbol{r} - \boldsymbol{r}_\alpha). \tag{S29}$$

Here τ, s respectively denote valley and spin indices, $\boldsymbol{K}_\tau = (\tau 4\pi/3a, 0)$, and $\phi_\alpha(\boldsymbol{r} - \boldsymbol{r}_\alpha)$ represent localized Wannier wavefunctions at lattice site $\boldsymbol{r}_\alpha$. The coefficients $c_{n,\tau,s}$ can be obtained from diagonalizing the tight-binding Hamiltonian in Eq. (S25) with the IVC order parameter now given by Eq. (S27). For bulk states, $c_{n,\tau,s}$ are expected to be uniform in real space, while for MZMs in a junction geometry they display an exponential decay with localization length ξ.

Substituting Eq. (S29) into Eq. (S28), the LDOS can be decomposed into two contributions: $\rho(E, \boldsymbol{r}) = \rho_0(E, \boldsymbol{r}) + \delta\rho(E, \boldsymbol{r})$. The first piece,

$$\rho_0(E, \boldsymbol{r}) = -\frac{1}{\pi}\text{Im}\sum_{\tau\tau',\boldsymbol{r}_\alpha} \text{tr}[G_{\tau\tau'}(\boldsymbol{r}_\alpha, \boldsymbol{r}_\alpha)] \times e^{i(\boldsymbol{K}_\tau - \boldsymbol{K}_{\tau'})\cdot\boldsymbol{r}_\alpha}|\phi(\boldsymbol{r} - \boldsymbol{r}_\alpha)|^2, \tag{S30}$$

involves Wannier orbitals at the same lattice site $\boldsymbol{r}_\alpha$, while the second, $\delta\rho(E,\boldsymbol{r})$, includes all contributions with Wannier orbitals evaluated at different lattice sites. In the equation above, $G_{\tau\tau'}(\boldsymbol{r}_\alpha,\boldsymbol{r}_\alpha)$ is a Green's function (the spin indices are omitted for simplicity) that can be directly calculated from the tight-binding Hamiltonian, Eq. (S25), using the recursive Green's function method [112, 113]. Since the relevant wavefunctions at the large D fields of interest are well-localized on one layer, and on one sublattice, the contribution from $\delta\rho(E,\boldsymbol{r})$ is expected to be significantly suppressed compared to $\rho_0(E,\boldsymbol{r})$; moreover, $\rho_0(E,\boldsymbol{r})$ already suffices to capture atomic-scale structure descending from IVC order. We therefore neglect $\delta\rho(E,\boldsymbol{r})$ hereafter.

To model the atomic orbitals, we consider Gaussian Wannier functions [79, 114]:

$$\phi(\boldsymbol{r}-\boldsymbol{r}_\alpha)=\frac{1}{\sqrt{2\pi}}e^{-\frac{(r-r_\alpha)^2}{2\sigma^2}}. \tag{S31}$$

In our simulations, we take $\sigma=0.3a$. Using this choice, the contribution $\delta\rho$ is indeed unimportant. Due to the large displacement field D, we expect the valence-band wavefunctions will be pushed onto the B_2 sites (or the A_1 sites for the opposite sign of the displacement field). Therefore, we position the Wannier centers of our tight-binding model on the B_2 sites, forming a triangular lattice.

As an illustration, Fig. S7(a-e) plots the atomically resolved wavefunction of extended bulk states with energy $E=1.2\Delta$, for various Kekulé angles θ. Unlike the Kekulé pattern for MZMs presented in the main text, here the patterns are translationally invariant—albeit with an enlarged unit cell reflecting IVC order. The main text Figs. 4(c-e) can thus be understood as a uniform Kekulé pattern at the corresponding Kekulé angle, superimposed on the additional spatial modulations coming from the exponentially decaying spatial profile of MZMs. There is a small asymmetry between the LDOS at y and $-y$ in the main text Figs. 4(c-e) arising from explicit breaking of mirror symmetry M_y in the low-energy theory. This breaking is manifest in the second term of Eq. (5), which arises from a combination of Ising SOC and trigonal warping. Figure S7(f) illustrates that, by similarly Fourier transforming the extended Kekulé bulk states, we obtain the usual Kekulé peaks in momentum space.